Supporting Information

Gerbal et al. 10.1073/pnas.1422534112

SI Text

1. SI Theory

A. Considerations on a Paramagnetic Ellipsoid Submitted to a Uniform Magnetic Field. See Fig. S1*A*.

In this section, we are considering an undeformable prolate ellipsoid of radii $r_{\parallel} > r_{\perp}$, respectively, along the main axis and in the other two orthogonal directions, only one of them being written in the forthcoming (see Fig. S1*A* for notations). The ellipsoid is assumed to be made of isotropic magnetic material. It is submitted to a uniform magnetic induction field $\overrightarrow{B_0} = \mu_0 \overrightarrow{H_0}$ with an incidence α relative to the main axis.

The magnetization inside such an ellipsoid submitted to a uniform field is constant. This result remains valid if the material is magnetically nonlinear with $\vec{M}$ following

$$\vec{M} = \chi(H)\vec{H}, \qquad [S1]$$

where $\vec{H}$ stands for the internal magnetic field. Expression **S1** may be seen as a definition for $\chi(H)$. In particular, it may follow a Langevin law: $\chi(H) = 3\chi_0 \mathcal{L}(aH)/aH \underset{H\to 0}{\longrightarrow} \chi_0$ where a is a constant, and $\mathcal{L}(x) = \coth(x) - (1/x) \simeq x/3 - (x^3/45)$.

Let β be the angle of $\vec{M}$ (and $\vec{H}$) relative to the ellipsoid main axis. The internal field depends on the geometry of the ellipsoid through the demagnetizing field, with the corresponding demagnetizing factors:

$$\vec{H} = \overrightarrow{H_0} + \overrightarrow{H_d} = \overrightarrow{H_0} - \bar{\bar{n}}\vec{M}, \qquad [S2]$$

where $\bar{\bar{n}} = \begin{pmatrix} n_{\parallel} & 0 \\ 0 & n_{\perp} \end{pmatrix}$ is a tensor of diagonal expression in the canonic reference frame of the ellipsoid. The demagnetization factors derive from the solution of the Maxwell equations:

$$n_{\parallel} = \frac{1-e^2}{e^2}\left[\frac{1}{2e}\ln\left(\frac{1+e}{1-e}\right) - 1\right], n_{\perp} = \frac{1-n_{\parallel}}{2} \text{ where } e = \sqrt{1 - \frac{r_{\perp}^2}{r_{\parallel}^2}}. \qquad [S3]$$

From Eqs. **S1** and **S2**, we may define an effective tensorial susceptibility:

$$\bar{\bar{\chi}}_e = \begin{pmatrix} \chi_{\parallel} & 0 \\ 0 & \chi_{\perp} \end{pmatrix} = \begin{pmatrix} \dfrac{\chi(H_{\parallel})}{1+n_{\parallel}\chi(H_{\parallel})} & 0 \\ 0 & \dfrac{\chi(H_{\perp})}{1+n_{\perp}\chi(H_{\perp})} \end{pmatrix}. \qquad [S4]$$

The infinite cylinder is a degenerate ellipsoid, for which we get $n_{\parallel} = 0$, $n_{\perp} = 1/2$, $\chi_{\parallel} = \chi(H_{\parallel})$, and $\chi_{\perp} = \frac{\chi(H_{\perp})}{1+\frac{\chi(H_{\perp})}{2}}$. No axial demagnetization takes place in the axial direction of the cylinder, so we also have $\chi_{\parallel} = \chi(H_{0\parallel})$.

Eqs. **S2** and **S4** may be combined to obtain a direct expression of $\vec{H}$ and $\vec{M}$ from $\overrightarrow{H_0}$:

$$\vec{M} = \bar{\bar{\chi}}_e \overrightarrow{H_0} = H_0 \begin{pmatrix} \chi_{\parallel}\cos\alpha \\ \chi_{\perp}\sin\alpha \end{pmatrix}, \qquad [S5]$$

$$\vec{H} = H\begin{pmatrix} \cos\beta \\ \sin\beta \end{pmatrix} = \overrightarrow{H_0} - \bar{\bar{n}}\vec{M} = H_0 \begin{pmatrix} \dfrac{\cos\alpha}{1+n_{\parallel}\chi} \\ \dfrac{\sin\alpha}{1+n_{\perp}\chi} \end{pmatrix}, \qquad [S6]$$

from which we can deduce the angle β (neglecting at this point the dependence of χ with H):

$$\tan(\beta) = \tan(\alpha)\frac{1+n_{\parallel}\chi(H_{\parallel})}{1+n_{\perp}\chi(H_{\perp})}. \qquad [S7]$$

Because $n_{\parallel}$ decays with increasing aspect ratio of the ellipsoid, Eq. **S7** indicates that in a high permeability material, the magnetization and the inside field tilts strongly toward the elongated axis, unless $\alpha = \pi/2$, in which case all of the fields are transverse. This is well illustrated in Fig. S1*B*, showing β, M, $M_{\parallel}$, and $M_{\perp}$ as a function of α in an infinite rod ($n_{\parallel} = 0$, $n\perp = 1/2$) corresponding to the experimental values of the nickel rods ($\chi_0 = 120$, $a = 10^{-3}\mathrm{A}^{-1}\mathrm{m}$) shown in Fig. S4*D*. All components of the magnetization are plotted with the same linear scale. With the exception of α very close to 90°, the magnetization is almost purely longitudinal. The variation of the magnetic energy potential (when χ is constant) is also plotted.

B. Energy and Torque for Nonlinear Magnetic Material. See Fig. S1*B*.

In our system, the temperature is set from an external thermostat and the magnetic induction field is imposed externally. Thus, from a thermodynamic perspective, the correct energy to be considered to search for equilibrium configurations is therefore the free magnetic enthalpy (1). Excluding also the energy of the void, its differential expression per unit volume is

$$dg_m = -sdT - \vec{M}.\overrightarrow{dB_0}, \qquad [S8]$$

where s is the entropy per unit volume and T the temperature. Integrating over a reversible transformation leads to $g_m = g_0(T) - \int_0^{B_0} \vec{M}.\overrightarrow{dB_0}$. Because for the ellipsoid the fields are uniform, the corresponding enthalpy of the whole volume V is simply $G_m = Vg_m$. If χ (and therefore $\bar{\bar{\chi}}_e$) is a constant, the integration is straightforward:

$$\begin{aligned} g_m &= g_0(T) - \mu_0 \int_0^{H_0} \bar{\bar{\chi}}_e \overrightarrow{H_0}.\overrightarrow{dH_0} \\ &= g_0(T) - \frac{\mu_0 H_0^2}{2}\left(\chi_{\parallel}\cos^2\alpha + \chi_{\perp}\sin^2\alpha\right). \end{aligned} \qquad [S9]$$

However, for a nonlinear magnetic material, the integral is not directly at hand. However, using Eq. **S2** we have $\vec{M}.\overrightarrow{dH_0} = \vec{M}.[\overrightarrow{dH} + d(\bar{\bar{n}}\vec{M})]$, where $\bar{\bar{n}}$ is constant. The integration of Eq. **S8** is thus possible again: $g_m = g_0(T) - \mu_0 \int_0^H MdH + (\mu_0/2)M.H - (\mu_0/2)\overrightarrow{H_0}.\vec{M}$ as in ref. 2. A further analytical calculation is possible. Integrating the latter equation by part yields

$$g_m = g_0(T) + \frac{\mu_0}{2}\int_0^H \frac{\partial\chi}{\partial H}H^2 dH - \frac{\mu_0}{2}\overrightarrow{H_0}.\vec{M}. \qquad [S10]$$

This expression corresponds to the magnetic term of the energy functional of the magnetic rod of the main paper. The equilibrium configuration is obtained through minimization with respect to the curvilinear angle $\theta(l)$ between the rod and the field. This is done here in the case of the ellipsoid for α:

$$\delta g_m = \frac{\mu_0}{2}\left[\frac{\partial \chi}{\partial H}\frac{\partial H}{\partial \alpha}H^2 - \frac{\partial\left(\overrightarrow{H_0}.\vec{M}\right)}{\partial \alpha}\right]\delta\alpha. \qquad \textbf{[S11]}$$

Eqs. **S5** and **S6** provide the expressions for each term between the brackets of Eq. **S11**: $H^2 = H_0^2\left[\left(\frac{\cos\alpha}{1+n_{\|}\chi(H_{\|})}\right)^2 + \left(\frac{\sin\alpha}{1+n_{\perp}\chi(H_{\perp})}\right)\right]^2$ and $\overrightarrow{H_0}.\vec{M} = H_0^2\left[\frac{\cos^2\alpha}{1+n_{\|}\chi(H_{\|})} + \frac{\sin^2\alpha}{1+n_{\perp}\chi(H_{\perp})}\right]$. Thus, its calculation yields three terms, in which those depending on $\partial\chi/\partial H$ cancel out. The remainder is the same as the result of a direct differential of Eq. **S9**:

$$\gamma_m = -\frac{\mu_0}{2}H_0^2\sin(2\alpha).\Delta\chi, \qquad \textbf{[S12]}$$

where $\Delta\chi = \chi_{\|} - \chi_{\perp}$. For the infinite cylinder, $\Delta\chi_{cyl} = \chi(H_{\|}) - \frac{\chi(H_{\perp})}{1+\frac{\chi(H_{\perp})}{2}}$.

The demonstration requires a last point for completion: to show that γ_m is indeed the torque per unit volume unit. This can be obtained by computing the fundamental expression of the torque $\vec{\gamma}_m = \vec{M}\wedge\overrightarrow{B_0}$ (valid for any source of magnetization and for any shape) which yields the same expression as in Eq. **S12**. Alternatively, it is possible to demonstrate thermodynamically that the torque does verify $\delta g_m = -\vec{\gamma}_m.\overrightarrow{\delta\alpha}$: an operator exerts a torque $\vec{\gamma}$ to rotate reversibly by an angle $\overrightarrow{\delta\alpha}$ a magnetic system $\mathcal{S}$ in an external magnetic field $\overrightarrow{B_0}$. At any moment during the transformation he must oppose the magnetic torque of the system: $\vec{\gamma} = -\overrightarrow{\gamma_m}$. The energy varies by the amount of work brought by the experimenter to the system: $\delta g_m = \delta W = -\overrightarrow{\gamma_m}.\overrightarrow{\delta\alpha}$. Considering that rotating the sample by $\overrightarrow{\delta\alpha}$ is equivalent to rotating the external field $\overrightarrow{H_0}$ by $-\overrightarrow{\delta\alpha}$, in the absence of other geometrical changes we get $\delta g_m = -\mu_0\vec{M}.\overrightarrow{\delta H_0} = -\vec{M}.(\overrightarrow{\delta\alpha}\wedge\overrightarrow{B_0}) = -\overrightarrow{\delta\alpha}.(\vec{M}\wedge\overrightarrow{B_0}) = -\overrightarrow{\delta\alpha}.\overrightarrow{\gamma_m}$.

C. Magnetic Influence of a Rod on Itself. See Fig. S1*C*.

The following calculation relies on the classical dipolar approximation (1) to compute the field $\vec{H}_{ind}$ induced by a magnetic moment $\vec{m}$ at a remote location $\vec{x}$:

$$\vec{H}_{ind} = \frac{1}{4\pi}\left[\frac{3\vec{x}(\vec{m}.\vec{x})}{x^5} - \frac{\vec{m}}{x^3}\right]. \qquad \textbf{[S13]}$$

We consider an infinite homogeneous cylinder of radius r in a uniform induction field $\overrightarrow{B_0} = \mu_0\overrightarrow{H_0}$.

In case *i*, the field is aligned with the rod main axis. According to the calculation on an ellipsoid above, it induces a magnetization $\overrightarrow{M_{\|}} = \chi(H_0)\overrightarrow{H_0}$. The magnetic moment of a section of length dx at the abscissa x is therefore $\overrightarrow{dm_{\|}} = \pi r^2\chi(H_0)\overrightarrow{H_0}dx$ and using Eq. **S13** it induces at $x=0$ a field $\overrightarrow{dH_{ind\|}} = (r^2\chi(H_0)\overrightarrow{H_0}dx)/2x^3$. Integrating now over the entire cylinder (except the induced portion) to obtain the influence of the rod magnetization on the cylinder portion of length $2r$ at $x=0$:

$$\vec{H}_{ind\|} = \frac{\chi(H_0)\overrightarrow{H_0}}{2}. \qquad \textbf{[S14]}$$

In case *ii*, the external field is orthogonal to the rod and induces a magnetization $\overrightarrow{M_{\perp}} = \chi_{\perp}(H_{\perp})\overrightarrow{H_0}$ and the elementary moment at x is thus $\overrightarrow{dm_{\perp}} = \pi r^2\chi_{\perp}(H_{\perp})\overrightarrow{H_0}dx$, which induces the following field at $x=0$: $\overrightarrow{dH_{ind\perp}} = -(r^2\chi_{\perp}(H_{\perp})\overrightarrow{H_0}dx)/4x^3$ because this time $\overrightarrow{H_0}.\vec{x} = 0$. Integration yields

$$\vec{H}_{ind\perp} = -\frac{\chi_{\perp}(H_{\perp})\overrightarrow{H_0}}{4} = -\frac{\chi(H_{\perp})}{1+\frac{\chi(H_{\perp})}{2}}\frac{\overrightarrow{H_0}}{4}. \qquad \textbf{[S15]}$$

Note that in case *i*, the field induced by the local section on itself is therefore $-(\chi(H_0)\vec{H}_0)/2$ because $H_{d\|} = 0$, and equals to $\vec{H}_{ind\perp}$ in case *ii* according to Eq. **S6**.

2. SI Plots of Theoretical Results

Plots of the theoretical deflections of the different models are shown in Fig. S2.

3. SI Independent and Axial Models Are Typical Landau Second-Order Transitions

Independent Model. For $\theta_0 = 0$, the deflection is $\delta = y(L) = \lambda_0\mathbf{Argcosh}(1/\cos\theta_L)$, but the integral expression is more convenient for the linearization: $\delta = \lambda_0\int_0^{\theta_L}\sin\theta d\theta/\sqrt{\sin^2\theta_L - \sin^2\theta} = \lambda_0\sin\theta_L\int_0^1 udu/(\sqrt{1-u^2}\sqrt{1-u^2\sin^2\theta_L})$, where $u = \sin\theta/\sin\theta_L$. For $\theta_L \ll 1$, the term $\sqrt{1-u^2\sin^2\theta_L}$ can be linearized under the integral. Using also $\int_0^1 udu/\sqrt{1-u^2} = 1$ and $\int_0^1 u^3du/\sqrt{1-u^2} = 2/3$, we obtain

$$\delta \simeq \lambda_0\sin\theta_L\left(1 + \frac{1}{3}\sin^2\theta_L + \ldots\right). \qquad \textbf{[S16]}$$

We also need the solution for θ_L which is provided by

$$\begin{aligned} L &= \lambda_0\int_0^{\theta_L}\frac{d\theta}{\sqrt{\sin^2\theta_L - \sin^2\theta}} \\ &= \lambda_0 F\left[\frac{\pi}{2}, \sin\theta_L\right] \underset{\theta_L\to 0}{\longrightarrow} \lambda_0\frac{\pi}{2}\left(1 + \frac{1}{4}\sin^2\theta_L + \ldots\right), \end{aligned} \qquad \textbf{[S17]}$$

where F designates the incomplete elliptic integral of the first kind. Eqs. **S16** and **S17** yield the result (also shown Fig. S3)

$$\delta \simeq 2\lambda_0\sqrt{\frac{2L}{\pi\lambda 0} - 1} \propto \sqrt{B_0 - B_c^i}. \qquad \textbf{[S18]}$$

Axial Model. The deflection in the axial model is $\delta = \lambda_2/\sqrt{\sin\theta_L}\int_0^{\theta_L}\sin\theta d\theta/\sqrt{\sin\theta_L - \sin\theta}$. Using again $u = \sin\theta/\sin\theta_L$ and $\int_0^1 udu/\sqrt{1-u} = 4/3$, and $\int_0^1 u^3du/\sqrt{1-u} = 32/35$:

$$\begin{aligned} \delta &= \lambda_2\sin\theta_L\int_0^1\frac{udu}{\sqrt{1-u}\sqrt{1-u^2\sin^2\theta_L}} \\ &\underset{\theta_L\to 0}{\longrightarrow}\frac{4}{3}\lambda_2\sin\theta_L\left(1 + \frac{4}{15}\sin^2\theta_L + \ldots\right) \simeq \frac{4}{3}\lambda_2\theta_L. \end{aligned} \qquad \textbf{[S19]}$$

Here, θ_L is provided by $L = \lambda_2/\sqrt{\sin\theta_L}\int_0^{\theta_L}d\theta/\sqrt{\sin\theta_L - \sin\theta} = \lambda_2\int_0^1 du/(\sqrt{1-u}\sqrt{1-u^2\sin^2\theta_L})$. By the same type of expansion as above and using $\int_0^1 du/\sqrt{1-u} = 2$, and $\int_0^1 u^2du/\sqrt{1-u} = 16/15$, we find

$$L \underset{\theta_L\to 0}{\longrightarrow} 2\lambda_2\left(1 + \frac{4}{15}\sin^2\theta_L + \ldots\right). \qquad \textbf{[S20]}$$

From Eqs. **S19** and **S20** we also find the critical exponent for the axial model (Fig. S3):

$$\delta \simeq \frac{4}{3}\lambda_2\sqrt{\frac{15}{4}\left(\frac{L}{2\lambda_2}-1\right)} \propto \sqrt{B_0 - B_c^a}. \qquad \textbf{[S21]}$$

4. SI Experiments with Nickel Rods: Shape Analysis and Determination of $\chi(H)$

See Fig. S4.

5. SI Experimental Setup for the Microrods

See Fig. S5.

6. SI Developments and Numerical Simulations Based on the Heuristic Model

A. Influence of the Variation of χ with H on the Buckling Threshold. The torque balance equation in the heuristic model is

$$\frac{C}{L}(\theta_L - \theta_0) = \pi r^2 L \frac{B_0^2}{2\mu_0}\Delta\chi \sin(2\theta_L). \qquad \textbf{[S22]}$$

With the hypothesis that $\chi \gg 1$ we can approximate $\Delta\chi \simeq \chi(H_\parallel)$ in the rest of this section.

If we first suppose $\chi = \chi_0$ to be a constant, when $\theta_0 = 0$ Eq. **S22** admits a nonzero solution for θ_L when the sin function increases faster than θ_L, which corresponds to $B_0 \geq B_c^h$ with $B_c^h = 1/rL\sqrt{\mu_0 C/\pi\chi_0}$ the critical threshold. Introducing $b = B_0/B_c^h$, Eq. **S22** can be rewritten in a dimensionless form:

$$\theta_L = \frac{b^2}{2}\sin(2\theta_L). \qquad \textbf{[S23]}$$

The buckling transition happens when the solution $\theta_L = 0$ becomes unstable—i.e., when the mechanical torque (left-hand term) increases slower than the magnetic term (right-hand term) upon a small perturbation. The derivative of Eq. **S23** yields $1 \leq b^2\cos(2\theta_L)$, corresponding indeed to $b^2 \geq 1$. After an expansion it is easy to show that the solution at the threshold follows the usual critical exponent: $\theta_L = \sqrt{3\delta_b}$, δ_b being a small variation of b above 1.

We consider now that $\chi(H) = (3\chi_0\mathcal{L}(aH))/aH$ with $\mathcal{L}$ the Langevin function (*SI Text*, section 1*A*). According to the supporting hypothesis of the heuristic model, here $H \simeq H_\parallel = \sin(\theta_L)H_0$.

Thus, using a Taylor expansion: $\chi(H) \simeq \chi_0(1 - (\theta_L a H_0)^2/15)$, Eq. **S23** is modified:

$$\theta_L = b^2\theta_L\left[1 - \theta_L^2\left(\frac{2}{3} + \gamma b^2\right)\right], \qquad \textbf{[S24]}$$

with $\gamma = 1/15(aB_c^h/\mu_0)^2$. As before, the derivative of this latter equation shows that the solution $\theta_L = 0$ ceased to be stable again for $b = 1$, indicating that the variation of χ does not change the buckling threshold. However, the equilibrium configuration does change after the transition, the bifurcation law being now $\theta_L = \sqrt{3\delta_b(1 - (3\gamma/2))}$. The interpretation is that a variation in the susceptibility happens only if H is large enough, which is not the case as long as the field incidence is transverse. However, once the rod has deflected, the susceptibility decays and therefore the rod bends less than if the material were magnetically linear.

B. Influence of Domains with a Permanent Moment on the Deflection of the Rod.

a. Modified torque balance equation of the heuristic model. We consider now that in addition to a paramagnetic susceptibility, the rod carries a permanent moment $\vec{S}$ with an orientation θ_s with respect to the direction of the rod main axis. In the external field $\overrightarrow{B_0}$ it induces a torque $\vec{S}\wedge\overrightarrow{B_0}$ on the rod. The rod equilibrium angle therefore depends on a modified torque equation: $(B_c^h)^2(\theta_L - \theta_0) = (B_0^2/2)\sin(2\theta_L) + SB_0\cos(\theta_L + \theta_s)$, which reads in its dimensionless form

$$\theta_L - \theta_0 = \frac{b^2}{2}\sin(2\theta_L) + bs\cos(\theta_L + \theta_s), \qquad \textbf{[S25]}$$

with $s = S/B_c^h$. The modification is straightforward if we now consider a set of n independent domains $\{s_i\}$ with a permanent moment oriented toward θ_s^i:

$$\theta_L - \theta_0 = f\frac{b^2}{2}\sin(2\theta_L) + b\sum_{i=1}^{n}\left[s_i\cos\left(\theta_L + \theta_s^i\right)\right]. \qquad \textbf{[S26]}$$

Here the dimensionless factor $0 < f < 1$ accounts for a relative reduction of the available paramagnetic quantity in the rod, assuming $f + \sum_{i=1}^{n} s_i = 1$.

b. Numerical simulations. The $\{s_i\}$ represents a set of permanent moments that would not comply directly with the external field excitation during the progressive magnetization of a sample. The presence of these domains in ferromagnetic materials is attested to by the Barkhausen effect, which can be seen (and heard) during a first magnetization curve. In the simulations, we assumed that these permanent moments are randomly oriented but with a mean orientation which depends on the demagnetization procedure: this latter could be performed either longitudinally or orthogonally to the rod (*Material and Methods*). So, the simulation consisted of initially choosing randomly each θ_s^i according to a Gaussian distribution $\mathcal{N}(\langle\theta_s^i\rangle, \sigma^2_{\theta_s^i})$, to check how the choices of $\langle\theta_s^i\rangle$ and $\sigma_{\theta_s^i}$ would influence the deflection of the rod along a first-magnetization curve. [By symmetry and for sake of simplicity we omitted the moments distributed around $\langle\theta_s^i\rangle + \pi$.]

In all simulations we initially fixed $f = 0.8$, $n \geq 10$, $s_i = 0.2/n$ and randomly chose θ_s^i along $\mathcal{N}(\langle\theta_s^i\rangle, \sigma^2_{\theta_s^i})$. Then we computed θ_L according to Eq. **S26** while the field b was incremented from zero as in the experiments. At each incremental step every "stuck" domain was tested to determine if it might "slip," i.e., quit its permanent "sticky" orientation and comply with the external excitations as the rest of the paramagnetic magnetization. This event corresponds to a Barkhausen jump. The criterion was $\Gamma_i = \mu_0|\vec{H}\wedge\overrightarrow{S_i}| \propto b \times s_i \sin(\theta_i^s - \beta)\sqrt{\left(\sin^2\theta_L + \frac{\cos^2\theta_L}{1+\frac{\chi_0}{2}}\right)} \overset{?}{\geq} \Gamma_t$, where $\vec{H}$ is the paramagnetic internal field and β its orientation with respect to the rod axis. The square root term is proportional to H (from Eqs. **S3** and **S6**). $\Gamma_t = 0.2$ is the arbitrarily user-fixed parameter which designs the slippage threshold. [Other criteria have been tried such as the $\overrightarrow{\Gamma_i} = \vec{S}\wedge\overrightarrow{B_0}$ as in Eq. **S25**. But, they did not yield results as satisfactory as the internal criterion retained.] In the simulation, if such a stick–slip happened, s_i was set to zero and f was increased by the same amount. The qualitative behavior of the simulation neither depends much on Γ_t, nor on n. The results of these simulations for various values of $\langle\theta_s^i\rangle$ and $\sigma_{\theta_s^i}$ are shown in Fig. 4, Movies S4–S6, and commented on in the main text.

1. Landau LD (1969) *Physique théorique. VIII, Électrodynamique des milieux continus* (MIR, Moscow).

2. Morozov KI, Engel A, Lebedev AV (2002) Shape transformations in rotating ferrofluid drops. *Europhys Lett* 58(2):229–235.

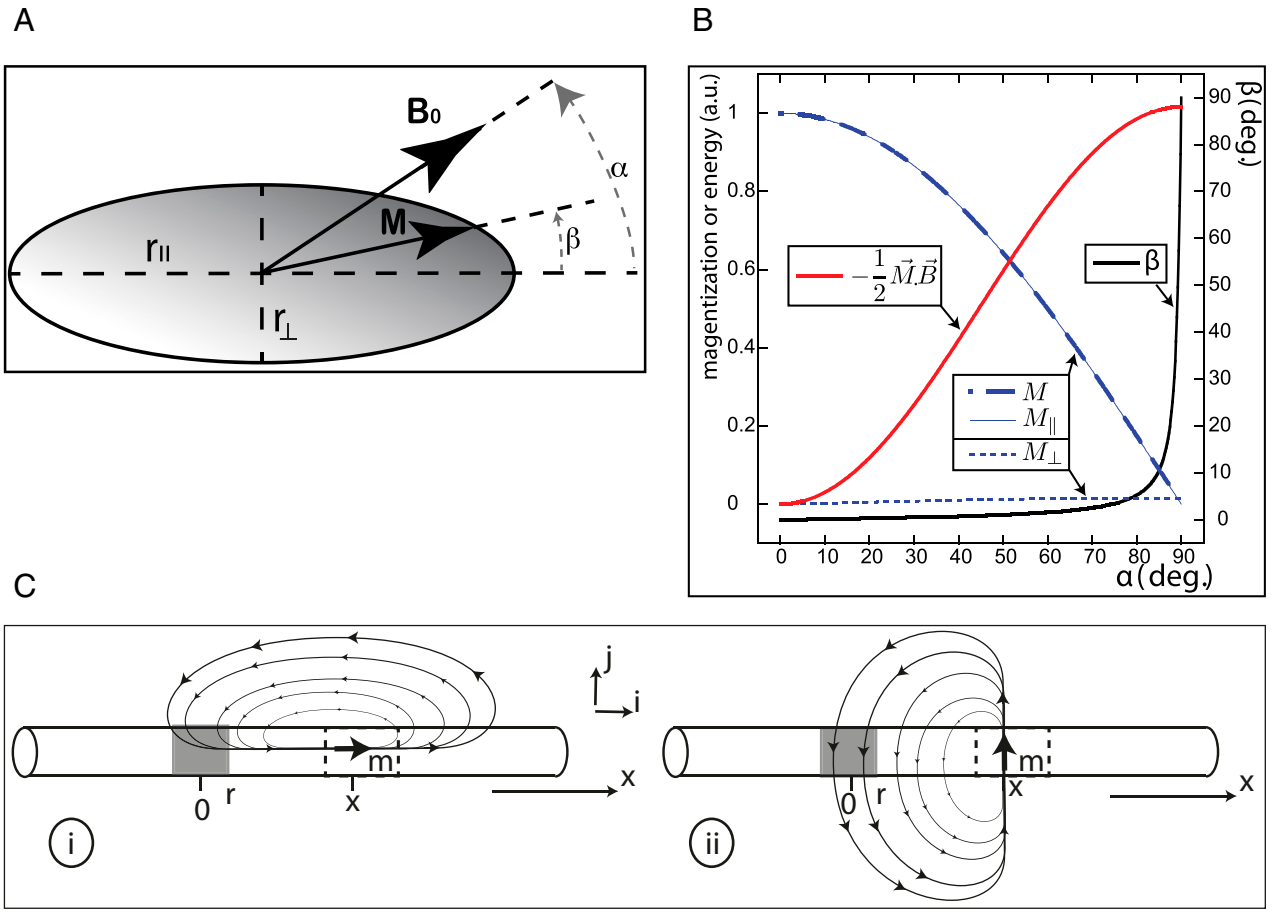

Fig. S1. (*A*) Notations for a magnetized ellipsoid in a uniform field. (*B*) Orientation and amplitude of the magnetization in an infinite cylinder as functions of the incidence of the external field. (*C*) Schema and notation for the calculation below: what is the influence of a magnetic moment $\vec{m}$ in the rod on another portion of the rod located at distance x? (*i*) When $\vec{m}$ is along the main axis of the rod; (*ii*) when $\vec{m}$ is transverse.

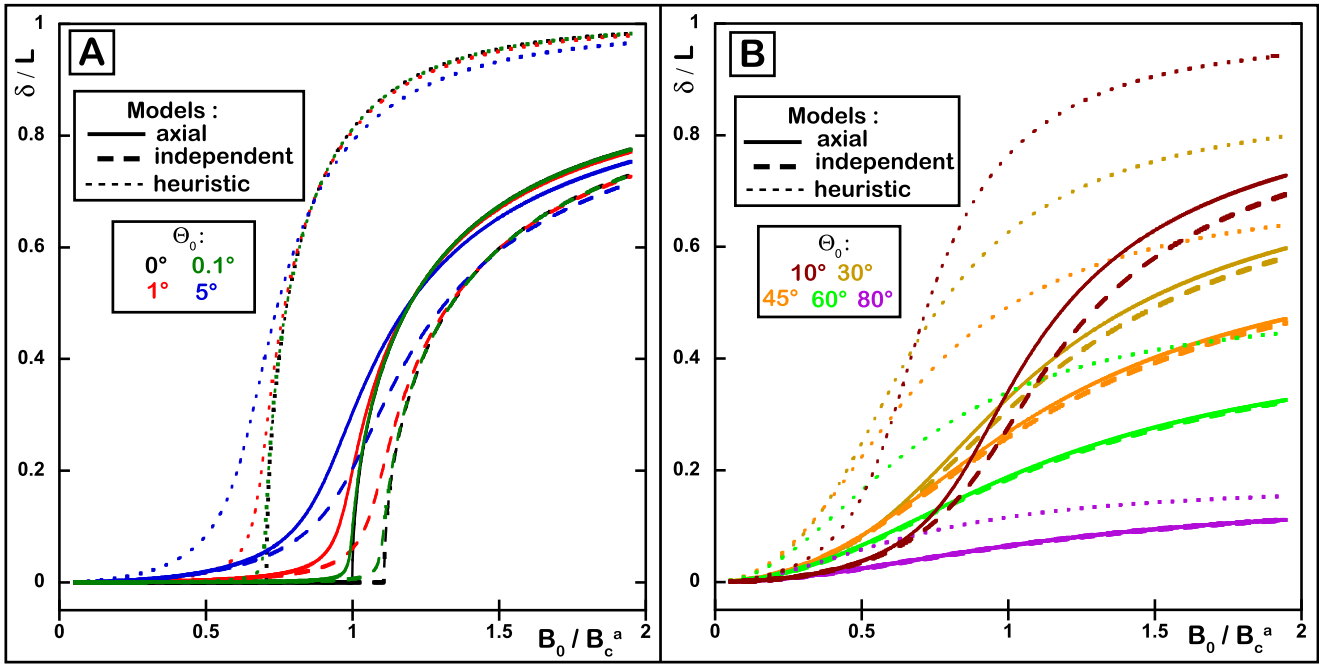

Fig. S2. Plots of the deflection of the tip (δ) of a rod of length $L = 1$ as a function of the external magnetic field B_0 relative to the critical field of the axial model (B_c^a). Results of computations from the independent model (solid lines), axial (long dashed lines), and heuristic models (short dashed lines) are shown. (*A*) Incidences of the field (θ_0) close to 0° (perpendicular to the rod axis) as indicated by color on the graph, and (*B*) for larger incidences from $\theta_0 = 10°$ to 80°.

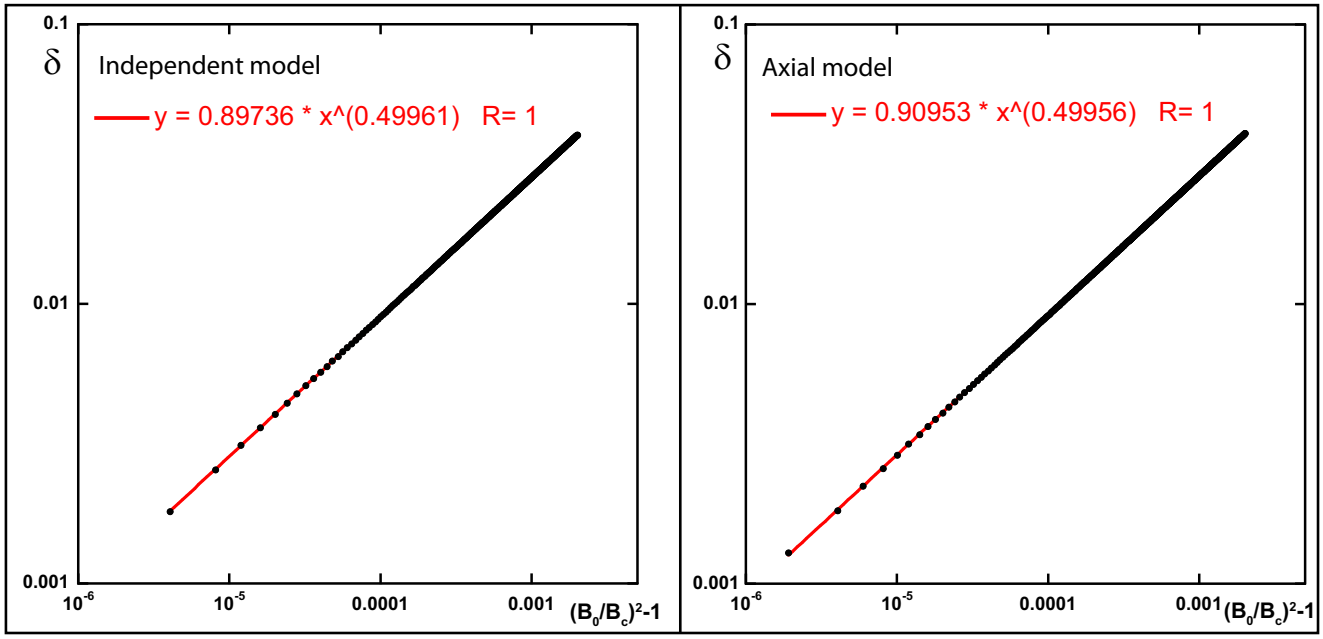

Fig. S3. Numerical calculation of the rod deflection δ for the independent and axial model at vicinity of the critical field. The power fit yields for both models an exponent 1/2 as expected in a transition of the second type. Alternatively to the numerical calculation, this result can also be obtained theoretically by linearization of the equations.

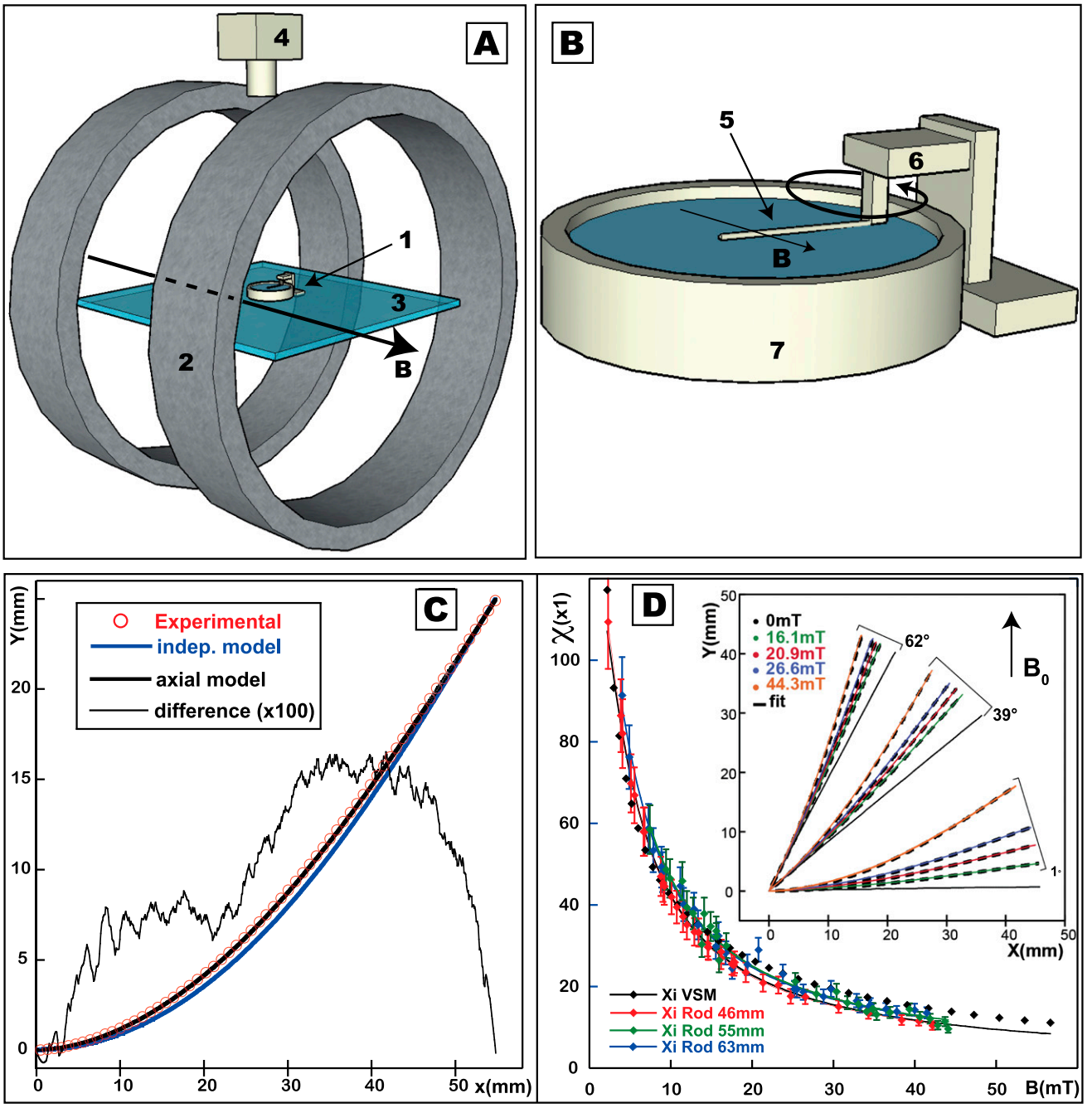

Fig. S4. (*A*) Experimental setup for the nickel rods. The sample (1) is set at the center of solenoid coils (2) in the Helmholtz configuration (ø = 70 cm), on a supporting board (3) and monitored from above with a still camera (4). (*B*) Enlarged view of the sample holder. The Ni rod (5) is clamped in a holder (6) which can be rotated to change the field incidence (angle monitored by the camera). To prevent vertical bending under their own weight, the longest rods lie at the surface of a water-filled dish (7). (*C*) Comparison between the experimental and theoretical shapes (axial model) of magnetically deformed Ni rods. Expanded view of the fitted rod of Fig. 2*A* (see main text). Parameters are L = 60.7 mm, B_0=26.6 mT, θ_0=1°. One-tenth of the digitized pixels has been plotted (red circles) and superimposed with the curve computed from the independent model (blue) and the axial model (black). Both are deduced from the deflection at the tip where the precision is the highest. The thin black curve indicates the difference between the experiment and the axial model (×100). The largest difference is of 165 μm at most (mean difference: 2.4%). Consistent with the wrong assumption that the local magnetization depends on the local external field, the independent model underestimates the axial magnetization at vicinity of the anchored point [largest difference is 825 μm (mean = 15%)], and thus also the bending. (*D*) Measures of the magnetic susceptibility [$\chi(H)$] as a function of B = μ_0 H deduced from the deflection of three different rods [L = 46 (red lozenges), 55 (green), and 63 mm (blue)]. To obtain the magnetization curve on a large range of values, we varied both the field intensity (from 0 to 44 mT) and its incidence (θ_0 ranging from 1 to 80°). Before each experiment the rods were demagnetized. We found no discrepancy in the measures performed at different angles (different combinations of θ_0 and field intensity may yield the same value for $H_{0\|}$). The data obtained by vibrating sample magnetometry (VSM) are also plotted (black lozenges). All data in the set were fitted by the function $\chi(B) = \chi_0(3\mathcal{L}(aB/\mu_0))/aB/\mu_0$ (solid colored lines), where $\mathcal{L}$ is the Langevin function. These fits returned for χ_0: 126 (VSM) data, 135, 138, and 133 for the three rods (respectively, by size order). (*Inset*) Digitized shapes of the 46-mm rod exposed to five field intensities (always oriented toward the top of the figure) for three values of θ_0 (indicated on the graph). For each shape the theoretical curve from the axial model is superimposed (dashed lines).

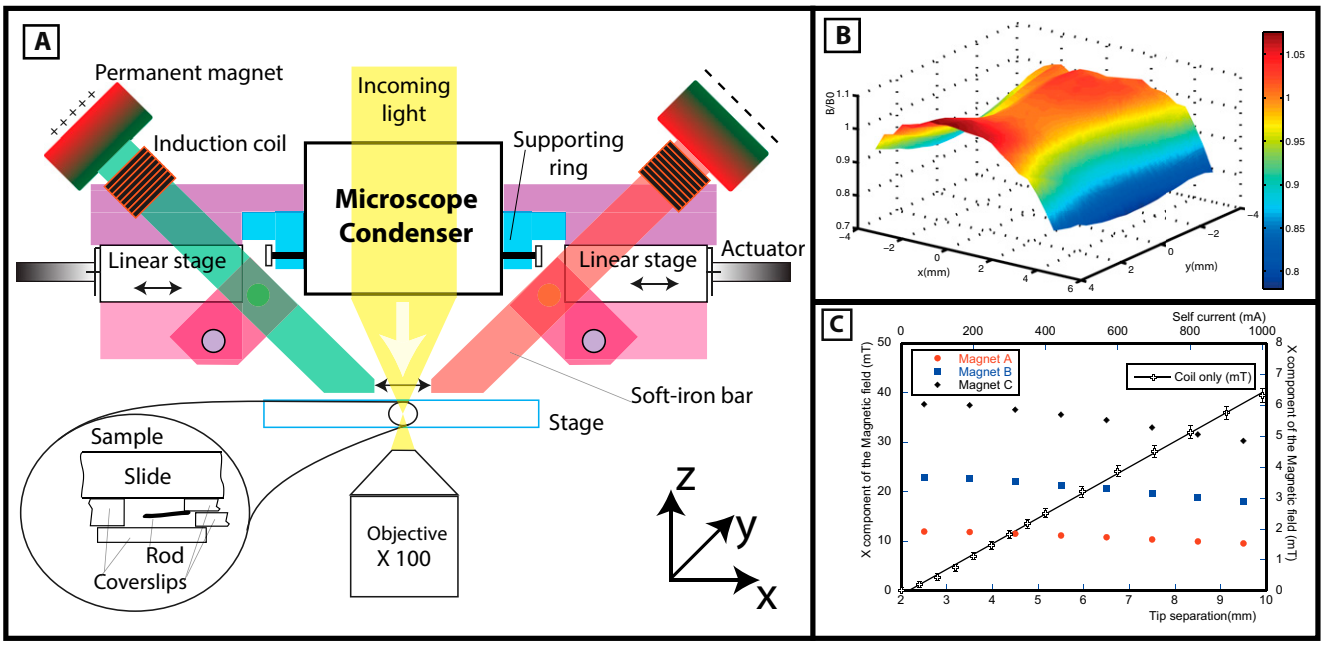

Fig. S5. Magnetic setup for the microrods. (*A*) Diagram of the setup: the magnetic system is axisymmetric and hangs on a ring fixed on the condenser of the inverted microscope. It consists of two 7-cm soft iron bars, planed at one end so they can be brought to the vicinity of the sample, mounted on microstage so their horizontal distance can be adjusted with a precision of 10 micrometers. The height of the apparatus could be adjusted by the rack of the microscope originally designed to adjust the condenser. The magnetic field was induced by putting permanent magnets at the remote end of these bars, each of them also being wrapped in an induction coil. The symmetry of the induction devices (magnets and coils) ensures that the field in the midperpendicular plane must be horizontal. A set of permanent magnets was used to reach strong magnetic field (~ 30 mT), which could be fine-tuned by the microstage. During an experiment, the coils were used to avoid mechanical disturbances and enable precise tuning of the field over a short period. Magnets and coils were also used to demagnetize the bars at the start of any experiment. The entire setup is free to rotate around the condenser. (*Inset*) Cross-section of the sample. (*B*) Three-dimensional representation of the spatial variation of the field between the tip iron bars. (See axis on *A*.) The *x* component of the field is plotted at the expected height of the rod. (*C*) Calibration of the *x* component of the field at the expected position of the sample. The field induced by three different magnets (left axis) as a function of the distance between the tip of the bars (bottom axis) is plotted when the induction coils are off-current. Alternatively, in the absence of permanent magnet, the magnetic field induced by the coils (right axis) is plotted as a function of the current intensity in the coil (upper axis) for a tip distance of 2.5 mm. Points are fitted by a regression line. Error bars are mostly due to the uncertainty of the field on the sample originating from the uncertainty in height (*Material and Methods*).

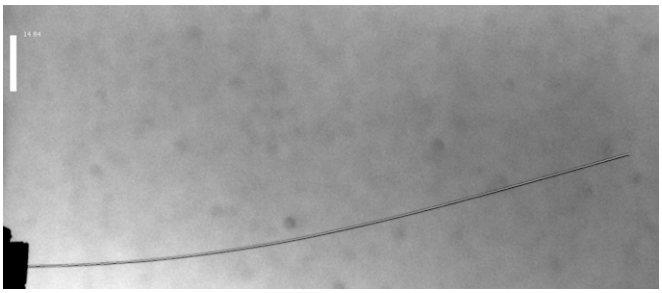

Movie S1. Nickel rod (63 mm) exposed to a magnetic field orthogonal to the undeformed rod (first and last image). Each picture of the movie is taken 1.5 s after the field intensity is changed, allowing the system to reach equilibrium. The bar represents the field intensity whose value is indicated in mT. The instability occurs between 13.73 and 13.95 mT. The white line on the rod is a plot of the automatic rod recognition performed by our software.

Movie S1

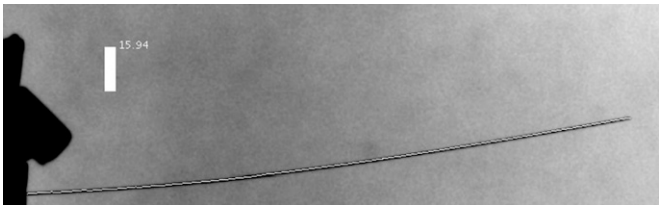

Movie S2. Nickel rod (40 mm) exposed to a magnetic field with an incidence of 2.40° relative to the orthogonal direction of the undeformed rod. Each picture of the movie is taken 1.5 s after the field intensity is changed, allowing the system to reach equilibrium. The bar represents the field intensity whose value is indicated in mT. The instability occurs between 14.61 and 14.84 mT. The white line on the rod is a plot of the automatic rod recognition performed by our software.

Movie S2

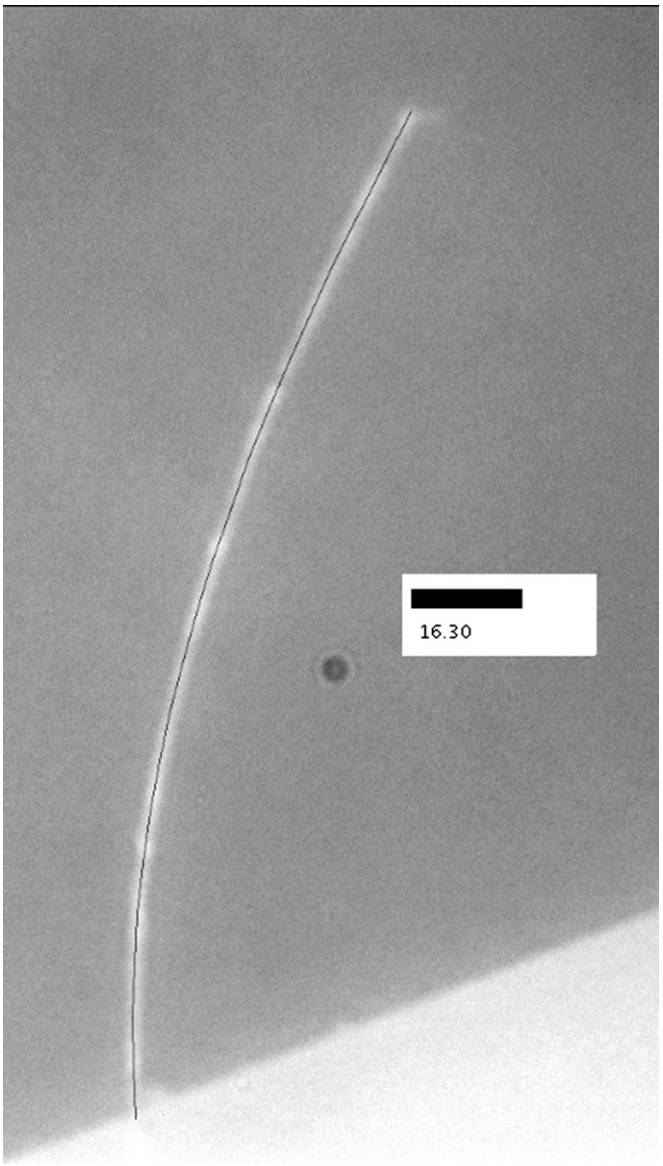

Movie S3. Superparamagnetic rod (42.3 μm long) in water exposed to an orthogonal magnetic field (to the undeformed rod). Each picture is taken for a 200-ms exposure time and 500 ms after the field intensity is changed. The bar represents the field intensity whose value is indicated in mT. At low field, only the thermal fluctuations are visible, and the bending starts only after the field reaches 10.8 mT. The dark line on the rod is a plot of the automatic rod recognition performed by our software.

Movie S3

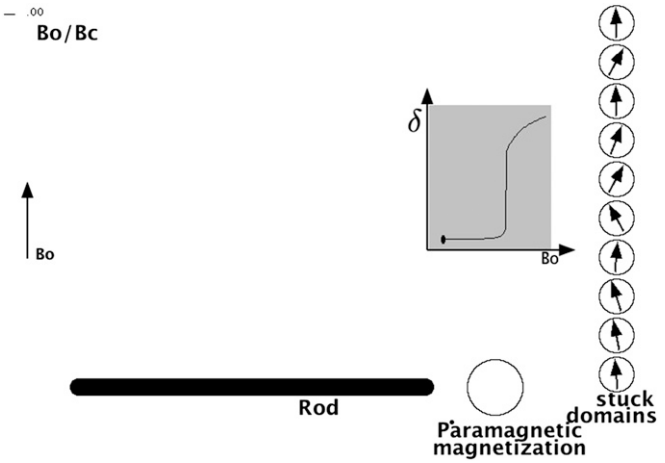

Movie S4. Results of simulation using the heuristic model complemented by a stick–slip description of 10 ferromagnetic domains stuck in random directions according to a Gaussian distribution (Fig. 4 of the main paper), and corresponding to 20% of the magnetic material of the rod. The movies indicate the deflection of the straight rod, hindered by a spring at its left end which is not represented. In the upper left corner the intensity of the vertical external field is drawn. The deflection of the rod is shown in the gray inset. The orientation (relatively to the external frame of reference) of the free paramagnetic magnetization in the rod is indicated by the arrow in the large circle whereas its magnitude is proportional to the bar on the left side of this circle. The orientation of each domain (of constant intensity) is shown on the right side of the movie. The arrows disappear when the domains slip. Each frame is plotted from the numerical solution of the model detailed in *Discussion and Analysis*, and corresponds to an equilibrium configuration. The slipping threshold was set at 0.2 and did not require fine-tuning to obtain the same qualitative behavior (from 0.1 to 1). The SD of the distribution of the domain angles is 20°. Initial configuration: the external field is orthogonal to the rod and the mean angle of the domain distribution is aligned with the field; a transition occurs slightly above the paramagnetic threshold.

Movie S4

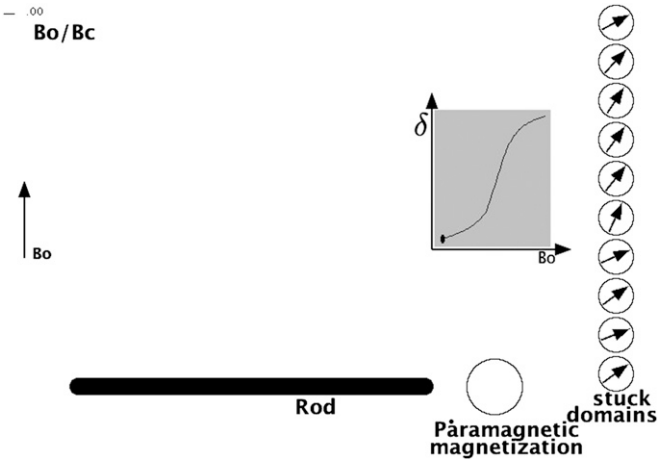

Movie S5. Results of simulation using the heuristic model complemented by a stick–slip description of 10 ferromagnetic domains stuck in random directions according to a Gaussian distribution (Fig. 4 of the main paper), and corresponding to 20% of the magnetic material of the rod. The movies indicate the deflection of the straight rod, hindered by a spring at its left end which is not represented. In the upper left corner the intensity of the vertical external field is drawn. The deflection of the rod is shown in the gray inset. The orientation (relatively to the external frame of reference) of the free paramagnetic magnetization in the rod is indicated by the arrow in the large circle whereas its magnitude is proportional to the bar on the left side of this circle. The orientation of each domain (of constant intensity) is shown on the right side of the movie. The arrows disappear when the domains slip. Each frame is plotted from the numerical solution of the model detailed in *Discussion and Analysis*, and corresponds to an equilibrium configuration. The slipping threshold was set at 0.2 and did not require fine-tuning to obtain the same qualitative behavior (from 0.1 to 1). The SD of the distribution of the domain angles is 20°. Initial configuration: the external field is orthogonal to the rod and the mean angle of the domain distribution has a 45° angle with the field (and the rod). No instability is seen, because the domains slip progressively.

Movie S5

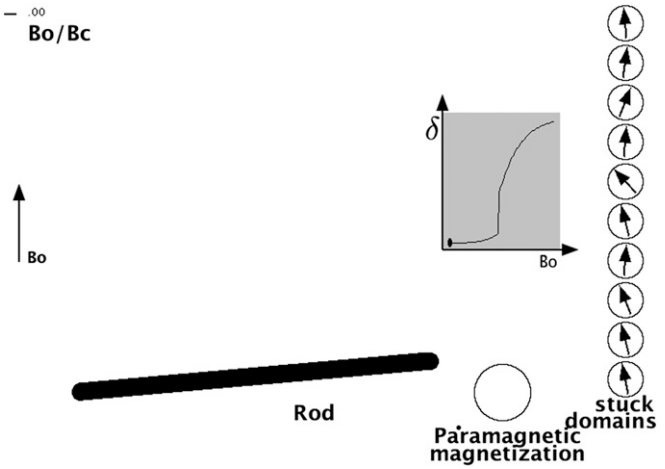

Movie S6. Results of simulation using the heuristic model complemented by a stick–slip description of 10 ferromagnetic domains stuck in random directions according to a Gaussian distribution (Fig. 4 of the main paper), and corresponding to 20% of the magnetic material of the rod. The movies indicate the deflection of the straight rod, hindered by a spring at its left end which is not represented. In the upper left corner the intensity of the vertical external field is drawn. The deflection of the rod is shown in the gray inset. The orientation (relatively to the external frame of reference) of the free paramagnetic magnetization in the rod is indicated by the arrow in the large circle whereas its magnitude is proportional to the bar on the left side of this circle. The orientation of each domain (of constant intensity) is shown on the right side of the movie. The arrows disappear when the domains slip. Each frame is plotted from the numerical solution of the model detailed in *Discussion and Analysis*, and corresponds to an equilibrium configuration. The slipping threshold was set at 0.2 and did not require fine-tuning to obtain the same qualitative behavior (from 0.1 to 1). The SD of the distribution of the domain angles is 20°. Initial configuration: the rod is tilted by 5° toward the field. The mean angle of the domain distribution is again mostly orthogonal to the rod and a transition is seen when the domains slip.

Movie S6